Visible-Light Integrated PIN Avalanche Photodetectors With High Responsivity and Bandwidth

Prithvi Gundlapalli, Victor Leong, Jun Rong Ong, Thomas Y. L. Ang, Salih Yanikgonul, Shawn Yohanes Siew, Ching Eng Png, *Senior Member, IEEE*, and Leonid Krivitsky

***Abstract*—Integrated photodetectors are key building blocks of scalable photonics platforms. Many recent improvements have been made for integrated avalanche photodetectors (APDs) operating at infrared telecommunications wavelengths, but their visible-spectrum counterparts remain relatively unexplored. Here, we demonstrate PIN-doped silicon APDs for visible light detection, monolithically integrated with a silicon nitride photonics circuit via end-fire coupling. An in-depth study of multiple PIN doping profiles reveals different optimal designs based on the desired operating regimes. At −49 dBm input power, they show 0.25 A/W (0.8 A/W) responsivity at reverse bias as low as 0.5 V (5.5 V), with corresponding dark current of <3 pA (50 pA). We also report fast RF response with an optimal 3 dB bandwidth of 11 GHz and gain-bandwidth product of 142 GHz, with all devices yielding open eye diagrams at 25 Gbps or above. Coupled with CMOS-compatible fabrication, our APDs will enable scalable photonics applications in sensing, communications, and quantum technologies at visible wavelengths.**

***Index Terms*—Avalanche photodiodes, optoelectronic and photonic sensors, photodetectors, photonic integrated circuits, silicon photonics.**

I. Introduction

INTEGRATED photonics are becoming increasingly important in numerous cutting-edge technologies, not only in high-speed communications and information technologies [1] but also in emerging quantum computing and quantum sensing devices [2], [3]. Much focus is now being placed on the integration of multiple photonics device elements such as light sources, modulators, and photodetectors into a single platform, as well as leveraging CMOS foundry capabilities for scalable fabrication and deployment [4], [5], [6].

Avalanche photodetectors (APDs) are an essential component of integrated photonics as they are fast, highly sensitive, and are compatible with established silicon photonics platforms [7]. Due to widespread applications in communications networks as high-speed interconnects, the development of integrated APDs has been largely focused on infrared telecommunications wavelengths [8], [9], [10], [11].

However, visible-spectrum integrated APDs have not been extensively developed, despite their numerous potential applications in visible-light communications [12], [13], bioimaging [14], [15], [16], quantum sensing [17], [18], quantum information [2], [19], [20], and LiDAR [21], [22]. Moreover, unlike superconducting detectors used in many quantum photonics demonstrations [23], [24], integrated APDs would not require cryogenic cooling [25], and thus are well-suited for developing systems for scalable deployment. A key technical challenge for the development of visible-light devices is the coupling of the APD to the input waveguide: while interlayer transitions are the common approach for infrared devices, it is challenging for visible wavelengths due to the long coupling lengths required, and may lead to trade-offs in noise and bandwidth performance [26]. However, we also note that several recent reports have utilized this approach at or near visible wavelengths [27], [28], [29].

Recently, our group demonstrated the first integrated APDs for visible light [26] based on doped silicon (Si) waveguides, where we developed an end-fire coupling interface to achieve efficient input coupling to a silicon nitride (SiN) photonics circuit. We found that devices with a lateral PN doping profile showed superior performance compared to an interdigitated PN doping profile. However, we were only able to study one lateral doping profile. Here, we extend the development of the visible-spectrum integrated APDs by performing an in-depth study of PIN doping profiles, which are widely used in Si-Ge integrated APDs for infrared wavelengths [30], [31], [32]. The magnitude of avalanche gain is closely related to the electric field strength, and thus the addition of an intrinsic region could enhance the APD responsivity by widening the high-field depletion region. However, the peak electric field strength would also be lowered, which might affect avalanche multiplication

Manuscript received 7 September 2022; revised 30 October 2022 and 12 December 2022; accepted 15 December 2022. Date of publication 23 December 2022; date of current version 17 April 2023. This work was supported in part by the Agency for Science, Technology and Research (A*STAR), Singapore under Grant #21709, and in part by both A*STAR and the National Research Foundation, Singapore through its Quantum Engineering Programme under Grant NRF2021-QEP2-03-P04. *(Corresponding author: Victor Leong.)*

Prithvi Gundlapalli, Victor Leong, and Leonid Krivitsky are with the Institute of Materials Research and Engineering, Agency for Science, Technology and Research (A*STAR), Singapore 138634 (e-mail: victor_leong@imre.a-star.edu.sg).

Jun Rong Ong, Thomas Y. L. Ang, and Ching Eng Png are with the Institute of High Performance Computing, Agency for Science, Technology and Research (A*STAR), Singapore 138632.

Salih Yanikgonul and Shawn Yohanes Siew are with the Advanced Micro Foundry, Singapore 117685.

Color versions of one or more figures in this article are available at https://doi.org/10.1109/JLT.2022.3231638.

Digital Object Identifier 10.1109/JLT.2022.3231638

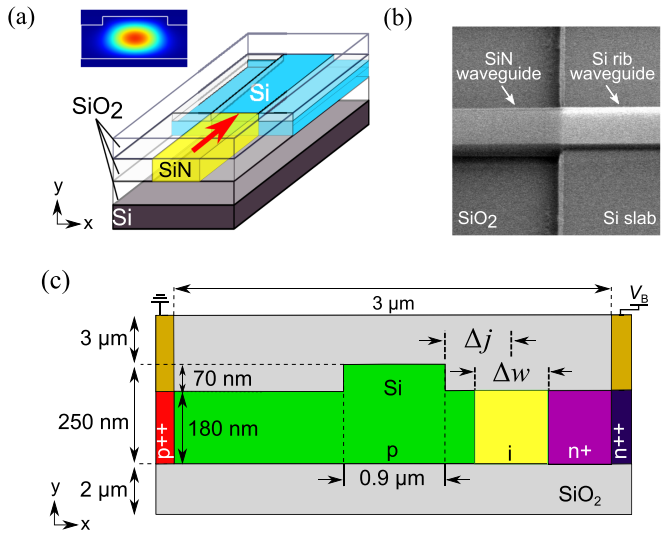

Fig. 1. Device structure and schematics. (a) Schematic of the APD device, showing the asymmetric Si rib waveguide end-fire coupled to an input SiN waveguide. The red arrow denotes the propagation direction of input light. The inset shows the simulated optical mode in the Si rib waveguide. (b) Scanning electron microscope (SEM) image of the Si-SiN coupling interface of a fabricated device, without the top SiO_2 cladding. (c) Cross-section schematic showing the doping profile of the Si rib waveguide. The intrinsic region has a width Δw, and its center is displaced by Δj from the right edge of the waveguide core.

efficiency [33]. Changes in the depletion region width, and hence junction capacitance, would also influence the bandwidth.

In this work, we explore numerous PIN doping profiles to find the optimal device design based on the performance metrics of dark noise, device responsivity, bandwidth, and eye diagrams. Besides generally strong performance based on these metrics across the device variants, we also show that the doping profiles can be optimized for different required operating regimes.

II. Device Design and Setup

The device design is shown in Fig. 1. The APD comprises of a Si rib waveguide of 16 μm length, sufficiently long for almost complete light absorption at visible wavelengths ($>99\%$ at 685 nm). The waveguide core width is 900 nm; the slab and rib heights are 180 nm and 70 nm, respectively. The device is cladded with 3 μm and 2 μm of SiO_2 above and below, respectively. We note that apart from ratio of the slab height to the overall waveguide height, the device dimensions follow that of the optimal design of our previous work [26].

The devices have a lateral p-i-n^+ doping configuration which is uniform over the length of the Si waveguide. Here, we study the variation of the width Δw of the intrinsic region, and the displacement Δj of its center from the edge of the waveguide core. In total, we investigate 16 device variants with Δw and Δj each having a value of 200, 300, 400, or 600 nm. The target n^+ (p) doping concentrations are 1×10^{19} (2×10^{17}) dopants/cm^3.

Electrical contacts are established via metal contacts on top of heavily doped p^{++} and n^{++} regions at the far ends of the 3 μm-wide Si slab.

We integrate the APD with a SiN photonics circuit via end-fire coupling to a rectangular SiN waveguide on the same device layer. The SiN waveguide dimensions match those of the Si waveguide core to minimize coupling losses, which are theoretically estimated to be <1 dB, limited mostly by Fresnel reflection losses [34]. Inverse-taper edge couplers with a minimum width of 150 nm allow for efficient light coupling from lensed optical fibers.

A. Device Fabrication

The devices were fabricated at Advanced Micro Foundry on an 8-inch silicon photonics platform. Starting with silicon-on-insulator (SOI) wafers with 340 nm Si thickness, the process flow is similar to our previous work [26], except that Si epitaxy was replaced with an etching process to obtain the required Si layer thickness.

We have tested over 100 devices across all design variants, chosen from different parts of the wafer. All tested devices were working and show repeatable results, indicating a robust and high-yield fabrication process.

B. Device Characterization

A full description of the characterization methods can be found in Appendix B. Briefly, a lensed fiber (2 μm spot diameter) delivers 685 nm continuous-wave (CW) laser light to the waveguides. The input light is horizontally-polarized, exciting the fundamental TE waveguide mode. Electrical probes establish electrical connections to on-chip contact pads.

Via cutback measurements [26], we obtain a total insertion loss of 3.1 ± 0.2 dB, consisting of the fiber-waveguide coupling loss (1.3 ± 0.1 dB), SiN waveguide propagation loss (~ 0.1 dB), and SiN-Si end-fire coupling loss (1.7 ± 0.2 dB). We obtain the input power P_{in} by subtracting the insertion loss from the optical power output of the lensed fiber.

III. Current-Voltage (I-V) Characteristics

We study the current-voltage (I-V) characteristics of the devices by measuring the device current I_{dev} while varying the reverse bias voltage V_{B} for different optical input powers P_{in}, as well as the dark current I_{dark} for $P_{\text{in}} = 0$. From the data, we calculate the responsivity $R = (I_{\text{dev}} - I_{\text{dark}})/P_{\text{in}}$. Results for a typical device with $\Delta w = \Delta j = 200$ nm are shown in Fig. 2(a).

In general, I_{dev} increases with V_{B}, and grows more sharply for $V_{\text{B}} > 10$ V (see Fig. 2(a)). This indicates greater avalanche multiplication as the applied bias approaches the breakdown voltage, which we define here as the reverse bias where I_{dark} reaches 0.1 mA. Unlike our previous PN-doped integrated APDs [26], the responsivity R of the current PIN-doped devices varies nonlinearly with increasing P_{in}, even for low V_{B} (see Fig. 2(b)). In particular, besides the responsivity saturating at large P_{in}, all device variants exhibit a positive nonlinearity — also referred to as supralinearity — at intermediate $P_{\text{in}} \sim -30$ dBm. This effect has been studied in other Si photodetectors [35], [36], [37], [38], and may be caused by higher optical powers increasing the filling

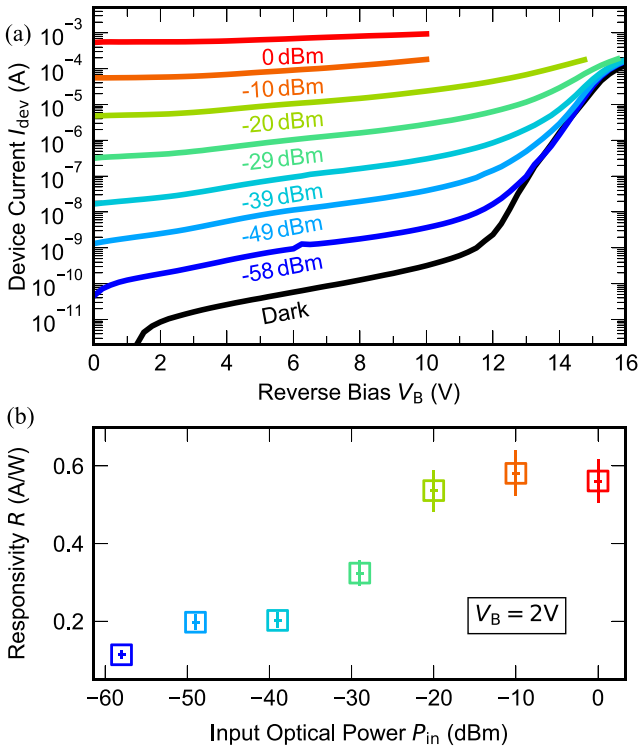

Fig. 2. Current-voltage (I-V) characteristics of a device with $\Delta w = \Delta j = 200$ nm. (a) Device current I_{dev} for varying reverse bias V_B at different input optical powers P_{in}. (b) Device responsivity $R = (I_{dev} - I_{dark})/P_{in}$ for varying P_{in} at $V_B = 2$ V. Insertion losses are accounted for in the reported P_{in} values. Error bars reflect uncertainties in fiber alignment, insertion losses, and input power.

of traps at the Si-SiO_2 interfaces, which decreases recombination losses.

We are unable to obtain data for $P_{in} < -60$ dBm due to difficulties in reliably measuring such low input optical powers in our setup. Nonetheless, using the responsivity values obtained at $P_{in} = -58$ dBm, we estimate that our devices have a minimum detectable power of $P_{in} \sim -70$ dBm, where I_{dev} approaches I_{dark}.

A. Comparing Different Doping Profiles

Next, we compare the I-V characteristics across all 16 device variants. Overall, the breakdown voltage increases with the intrinsic region width Δw due to lower peak electric fields across a wider depletion region. For a fixed Δw, we observe consistent trends related to the intrinsic region displacement Δj. We focus here on the results for $P_{in} = -49$ dBm, as shown in Fig. 3, though we note that the observed trends hold for other input powers.

For low reverse bias $V_B < 10$ V, all devices have similarly low dark currents I_{dark}, with $I_{dark} \sim 10$ pA at $V_B = 2$ V, increasing to ~ 100 pA or less at $V_B = 8$ V.

With input light, devices with a smaller Δj yield a larger I_{dev} (and responsivity R) even at zero bias. This is likely due to the optical mode in the Si waveguide having a larger overlap with the depletion region when it is less displaced from the center of the waveguide, leading to greater interaction of the photogenerated charge carriers with the higher electric fields. As such, we do not focus on the device "gain," typically defined as the ratio of the responsivity at a target bias to that at zero or low bias: since the responsivities are different even at zero bias, a larger gain does not necessarily imply an overall larger device response.

At high reverse bias $V_B > 10$ V, the trend is reversed, and devices with larger Δj show a larger I_{dev} and a lower breakdown voltage. With the depletion region displaced further away from the waveguide core, the photogenerated charge carriers travel a longer distance over which impact ionization can occur, leading to greater avalanche multiplication. This effect would be more significant at higher bias, and also agrees with the results of Geiger-mode simulations for single-photon detection where the devices are biased beyond the breakdown voltage [33].

B. Optimal Device for Different Bias Ranges

In practice, it is advantageous to operate the APDs at a lower reverse bias V_B, assuming the responsivity is not sacrificed. The benefits include lower dark noise, lower power consumption, as well as cost-effectiveness in producing the required bias voltage. Here, for a given input power of $P_{in} = -49$ dBm, we consider two use cases with different target responsivities R of 0.25 A/W and 0.8 A/W, corresponding to a lower and higher range of operating bias that is not too close to the breakdown voltage. The optimal device is then the one that achieves the target responsivity at the lowest bias V_B. We focus here on devices with $\Delta j = 200$ nm (see Fig. 4), having shown above that these devices show the highest responsivities except at high V_B near breakdown. We also consider the power consumption levels in the "standby" and "on" states, where "standby" power dissipation is given by the dark current only, and "on" state assumes constant continuous-wave input.

For the lower responsivity of $R = 0.25$ A/W, the largest intrinsic region width $\Delta w = 600$ nm gives the lowest required bias of $V_B = 0.5$ V with $I_{dark} < 3$ pA. This also reflects the effect of larger overlap of the depletion region with the optical mode, as mentioned above. The "standby" and "on" power consumption levels would be <1.5 pW and 1.6 nW, respectively. On the other hand, for the higher responsivity of $R = 0.8$ A/W, it is the smallest $\Delta w = 200$ nm that gives the lowest required bias of $V_B = 5.5$ V with $I_{dark} = 50$ pA. This seems to indicate that the higher peak electric field of a narrower depletion region induces a greater device response in this bias range. This device would consume for 0.28 nW and 55 nW for "standby" and "on" states, respectively.

Thus, choosing an optimal device design would depend on the operating conditions and requirements. A full set of data for all device variants can be found in Appendix A.

C. Comparison With PN-Doped Device

Here we compare a representative PIN-doped device ($\Delta w = \Delta j = 200$ nm) with a PN-doped device similar to those reported in our previous study [26]. Both device types have almost identical waveguide dimensions (900 nm width, 250 nm height), except that the PN device has a symmetric rib waveguide, with both slab and rib heights being 125 nm.

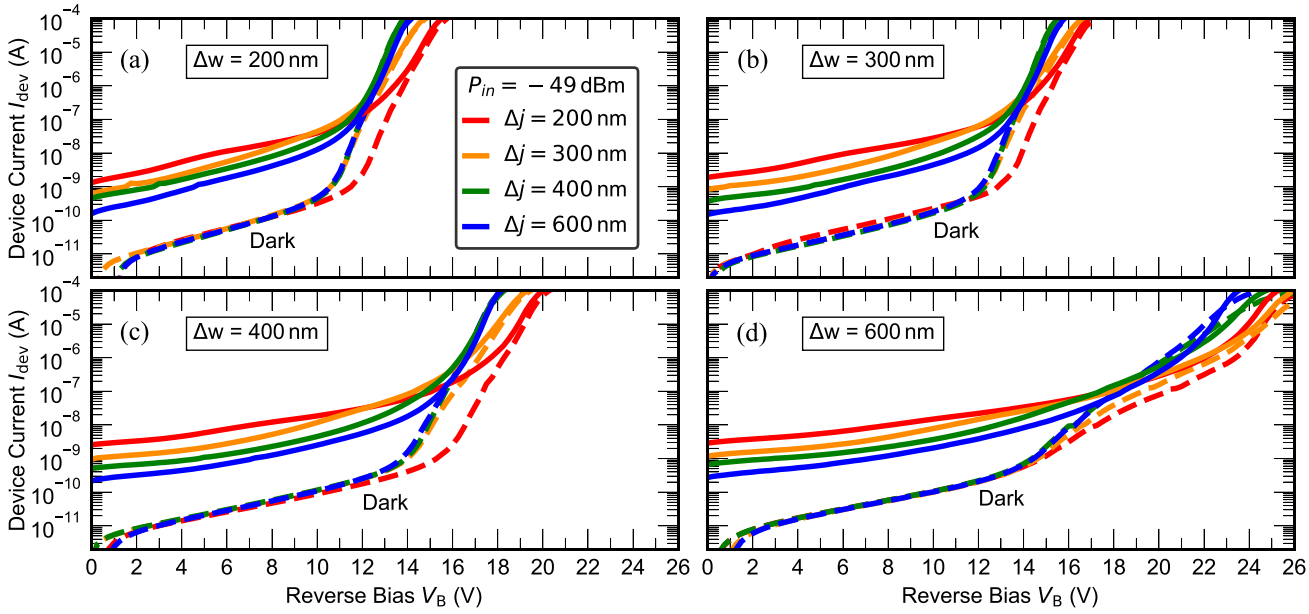

Fig. 3. Current-voltage (I-V) characteristics of all device variants. Each subfigure shows devices with the same intrinsic region width Δw, but different intrinsic region displacement Δj. Solid lines show measurements with input optical power $P_{\text{in}} = -49$ dBm (after accounting for insertion losses); dashed lines show dark current I_{dark}. All subfigures share the same legend.

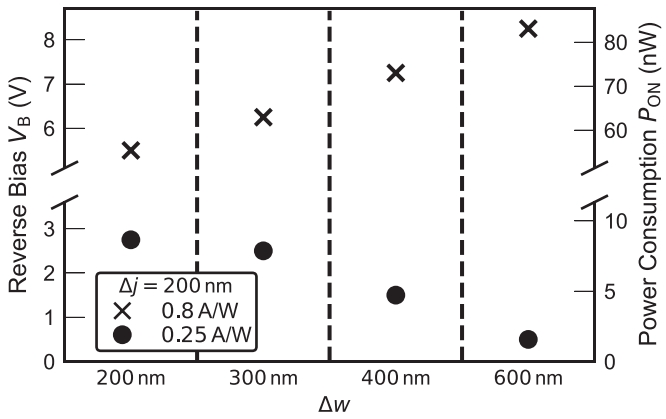

Fig. 4. Reverse bias voltage V_{B} required to achieve two target responsivities for devices with $\Delta j = 200$ nm, under a constant input power of $P_{\text{in}} = -49$ dBm. The corresponding power consumption P_{ON} is also shown. For the devices in this plot, the power dissipation due to dark current contributes negligibly to P_{ON} (see also Table II).

However, we do not expect this to significantly influence our comparison.

From the I-V characteristics shown in Fig. 5(a), the PIN device has a lower current response I_{dev} across a range of input powers P_{in}, but also has a lower dark current I_{dark}. Hence, for a more meaningful comparison, we discuss the signal-to-noise ratio $\text{SNR} = (I_{\text{dev}} - I_{\text{dark}})/I_{\text{dark}}$ of the two devices (see Fig. 5(b)). For a low $P_{\text{in}} = -58$ dBm, the PN device generally has a higher SNR than the PIN device. At higher P_{in}, we observe a high-bias regime at $V_{\text{B}} > 10$ V where the PIN device performs better than the PN counterpart; both devices have comparable SNR at lower bias. We note that in general, SNR decreases for high V_{B} near the breakdown voltage as the avalanche gain of dark current starts to become dominant.

As the PIN devices exhibit low I_{dark} and high SNR, they could be a more suitable choice for applications that are sensitive to dark current levels and passive power consumption, such as optical power monitors in integrated photonic circuits [39], [40].

IV. RF Performance

To characterize the RF response of the devices, we modulate the input light and measure the frequency-dependent device current at different reverse bias voltages V_{B} (see Fig. 6(a)). We then extract the 3 dB bandwidth, which we define with respect to a reference frequency of 1 GHz, as well as the gain-bandwidth product (GBP).

Fig. 6(b) and (c) compare the 3 dB bandwidth and GBP, respectively, of devices with varying intrinsic region width Δw; we do not observe any significant influence of the intrinsic region displacement Δj on the RF response. We observe the bandwidth increasing with V_{B} due to a larger bias widening the depletion region and lowering the junction capacitance. However, we do not observe the same trend with increasing Δw, as the bandwidth and GBP become lower. This could indicate that across these wider depletion regions, the bandwidth becomes transit-time limited [41], due to lower electric fields leading to slower drift velocities.

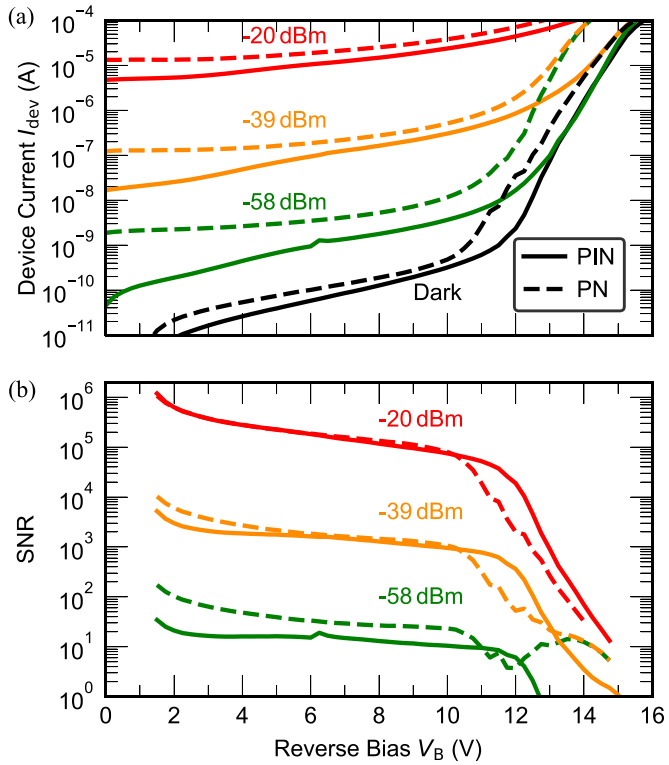

Fig. 5. Comparison of I-V characteristics of a PIN-doped device ($\Delta w = \Delta j = 200$ nm) with a PN-doped device of similar structure and design [26]. (a) The device current I_{dev} for three different input powers P_{in}, as well as the dark current I_{dark}. (b) The signal-to-noise ratio SNR $= (I_{dev} - I_{dark})/I_{dark}$. Data for $V_B < 1.5$ V is not shown as I_{dark} is below the measurement noise floor.

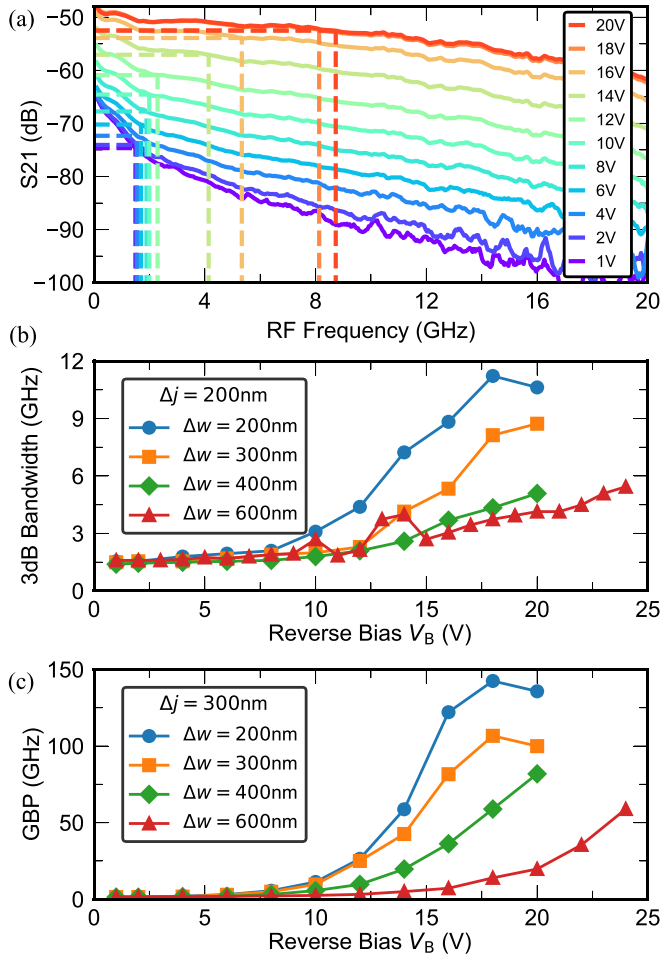

Fig. 6. RF performance of the PIN devices. (a) RF response at different reverse bias V_B for a device with $\{\Delta w, \Delta j\} = \{200, 300\}$ nm. Dashed lines indicate the 3 dB rolloff point with respect to the reference frequency of 1 GHz. (b) 3 dB bandwidth for devices with $\Delta j = 200$ nm. (c) Gain-bandwidth product (GBP) for devices with $\Delta j = 300$ nm. The input power is $P_{in} = -7.4$ dBm for all plots in this figure.

From Fig. 6(b) and (c) we see that the bandwidth and GBP do not appear to have saturated yet for $\Delta w = 400$, 600 nm devices at $V_B = 20$, 25 V. However, we do not measure at even higher bias as the devices would then be in the breakdown regime, where the noise is high due to dark current amplification, and the high-speed response would also be limited by avalanche buildup time [40], [42].

The highest 3 dB bandwidth of 11 GHz is measured for a device with $\{\Delta w, \Delta j\} = \{200, 200\}$ nm, while the largest GBP of 142 GHz is achieved by a device with $\{\Delta w, \Delta j\} = \{200, 300\}$ nm.

We also measured eye diagrams to demonstrate the high-speed communications capabilities of our devices. Despite the differences in bandwidth and GBP, all device types show open eyes up to at least 25 Gbps, but not above 35 Gbps; a typical result is shown in Fig. 7. There are no obvious trends between variations of Δw or Δj.

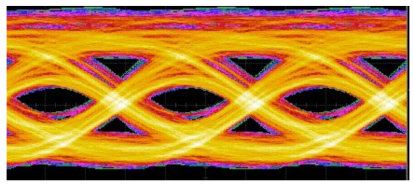

Fig. 7. Open eye diagram at 25 Gbps for a device with $\{\Delta w, \Delta j\} = \{200, 300\}$ nm, measured with $P_{in} = 1.1$ dBm. All devices show open eye diagrams up to 25 Gbps or higher.

V. Benchmarking

In Table I, we benchmark the performance of our devices against other recent reports of integrated APDs. We do not restrict the comparison to only visible-spectrum devices, but also include those operating at infrared wavelengths, though we note that our list is not exhaustive. A more detailed comparison with the PN-doped devices from our previous work [26] is given in Section III above.

Compared with other APDs, our devices exhibit strong performance as they have high responsivity R and low dark current I_{dark}. While the 3 dB bandwidth and GBP are somewhat lower than the highest values in the table, our devices could still be advantageous for applications where low noise and power consumption are more critical than very high speeds, such as in imaging and sensing.

TABLE I
BENCHMARKING OF DEVICE PERFORMANCE AGAINST OTHER RECENT REPORTS OF INTEGRATED APDS

Type	λ (nm)	R (A/W)	I_{dark} (nA)	BW (GHz)	GBP (GHz)	Device/Ref.
End-fire SiN/SOI, PIN	685	0.8 @ 5.5 V	0.05 @ 5.5 V	11 @ 18 V	98 @ 18 V	$\{\Delta w, \Delta j\} = \{200, 200\}$ nm
End-fire SiN/SOI, PIN	685	0.8 @ 7.25 V	0.1 @ 7.25 V	8.8 @ 18 V	142 @ 18 V	$\{\Delta w, \Delta j\} = \{200, 300\}$ nm
End-fire SiN/SOI, PN	685	0.83 @ 2 V	$\sim$0.001 @ 2 V	19.1 @ 20 V	234 @ 20 V	[26]
SiN-on-Si mesa, PN	405	[a]0.15 @ 13.3 V	[a]200 @ 13.3 V	[a]3.8 @ 13.3 V	173 @ 13.3 V	[27]
Si-on-SiN, PIN	775	0.19 @ 3 V	0.107 @ 3 V	6 @ 3 V	68 @ 45 V	[28]
SiN-on-SOI, PIN	850	0.29 @ 20 V	75 @ 20 V	14 @ 20 V	[a]20.3 @ 20 V	[43]
SOI, PIN	850	0.3 @ 14 V	2000 @ 14 V	6 @ 14 V	[a]98.4 @ 14 V	[44]
GaAs quantum dot	1310	0.04 @ 4 V	[a]60 @ 4 V	20 @ 15 V	585 @ 17 V	[45]
Ge/Si	1310	0.64 @ 2 V	10 @ 2 V	27 @ 12 V	300 @ 12 V	[8]
Ge/Si	1310	0.93 @ 4.7 V	4.5 @ 4V	48 @ 14 V	615 @ 14 V	[46]
Ge/Si	1550	0.78 @ 2 V	10 @ 2 V	[a]33.8 @ 13 V	[a]274 @ 13 V	[8]
Ge/Si	1550	0.8 @ 7 V	[a]200 @ 7 V	20.7 @ 10.6 V	232 @ 11.6 V	[11]
Ge/Si	1550	1.12 @ 3.6 V	[a]20 @ 3.6 V	[a]25 @ 9.8 V	[a]497 @ 9.8 V	[10]
InGaAs/InAlAs/Si	1570	0.99 @ 47 V	[a]7.6 @ 56 V	-	-	[47]

λ: operating wavelength, R: responsivity, I_{dark}: dark current, BW: 3 dB bandwidth, GBP: gain-bandwidth product. [a]These values were not explicitly reported, and were inferred from the figures or other values. Voltage value after @ indicates applied reverse bias.

VI. CONCLUSION

We have reported visible-light APDs based on Si rib waveguides with PIN doping profiles that are integrated with a SiN photonics circuit. The devices are fabricated at a commercial Si photonics foundry with a CMOS-compatible process. A systematic characterization of multiple device designs at 685 nm has identified optimal doping profiles for different operating bias voltage ranges: At -49 dBm input power, responsivities of 0.25 A/W (0.8 A/W) can be achieved at low reverse bias of 0.5 V (5.5 V), with a corresponding dark current of <3 pA (50 pA). The highest bandwidth and GBP are 11 GHz and 142 GHz, respectively, and the devices show open eye diagrams at 25 Gbps or above.

Our PIN devices show strong performance, including better SNR in some operating regimes, when compared to PN devices with similar waveguide designs detailed in our recent report [26].

Given that the doping profile design is a significant determining factor of APD performance, our in-depth study is a valuable contribution to the development of integrated APDs for visible light, and could also provide insights for improving integrated APDs based on other material platforms for other wavelengths. Moreover, this study provides an important milestone in advancing towards Geiger-mode operation for single-photon counting. Preliminary testing has shown that further optimization of device design and fabrication processes is required for stable, low-noise Geiger-mode operation. The advent of CMOS-compatible visible-spectrum integrated single-photon detectors would pave the way for widespread deployment of such devices in integrated quantum photonics platforms for applications in quantum communications, photonic computing, and quantum sensing.

APPENDIX A
REVERSE BIAS VOLTAGE V_{B} FOR DIFFERENT TARGET RESPONSIVITIES

Table II shows the reverse bias V_{B} required for achieving two target responsivities R of 0.25 A/W and 0.8 A/W for all 16 device variants, with their different values of intrinsic region width Δw and its displacement from the waveguide core Δj. The input power is $P_{\text{in}} = -49$ dBm. We also include the power consumption for both "standby" and "on" conditions, as described in the main text.

TABLE II
REVERSE BIAS V_{B} AND POWER CONSUMPTION AT TWO DIFFERENT TARGET RESPONSIVITIES

		R=0.25 A/W			R=0.8 A/W		
Δw (nm)	Δj (nm)	V_{B} (V)	P_{ON} (nW)	P_{SB} (nW)	V_{B} (V)	P_{ON} (nW)	P_{SB} (nW)
200	200	2.75	8.9	0.039	5.50	55	0.26
300	200	2.50	7.8	0.032	6.25	62	0.36
400	200	1.50	4.7	0.0075	7.25	74	0.27
600	200	0.50	1.6	<0.0015	8.25	84	0.51
200	300	4.75	15	0.16	7.25	71	0.72
300	300	5.50	17	0.17	8.50	86	0.82
400	300	6.50	21	0.22	9.75	103	1.0
600	300	6.75	21	0.26	10.75	106	1.4
200	400	5.75	18	0.26	8.50	87	1.4
300	400	8.00	27	0.57	10.25	98	1.9
400	400	9.00	28	0.73	11.75	116	2.7
600	400	9.50	30	0.87	13.00	139	4.6
200	600	7.50	25	0.77	9.75	104	3.7
300	600	9.25	30	1.2	11.50	114	5.5
400	600	10.75	36	1.6	13.25	143	7.6
600	600	11.50	38	2.0	17.00	634	461

P_{ON}, P_{SB}: "On" and "standby" power consumption, respectively.

In Section III, we highlight the case for $\Delta j = 200$ nm, where the required V_{B} to achieve the lower target of $R = 0.25$ A/W decreases with a larger Δw. We note that this trend reverses for values of $\Delta j >= 300$ nm.

The trend for the higher target of $R = 0.8$ A/W is consistent for all Δj values: the required V_{B} increases with Δw.

APPENDIX B
CHARACTERIZATION METHODS

A. Current-Voltage (I-V) Measurements

Measurements of DC characteristics are typically performed with DC electrical probes, but we use RF probes here for practical reasons: to minimize the changing of probes in the setup across different lab users.

Each RF probe (Formfactor Infinity, GSG, 67 GHz) contacts one of the pads (P or N) with the signal (S) pin; the ground (G) pins rest on the SiO_2 cladding. The coaxial RF probes are connected to a sourcemeter (Keithley 2636B) via a triax-to-coax adapter (guard disconnected). The noise floor is dominated by the leakage current in the coaxial segments (RF probes and coax cables). To minimize noise, the adapter is placed close to the probes, with the coaxial cable length kept short (55 cm). The resultant noise floor is < 2 pA.

For I-V measurements, the reverse bias voltage V_B is swept from 0 V up to a threshold voltage where the device current I_{dev} exceeds a limit of 200 μA. We note that this current limit is slightly higher than threshold of 100 μA used to define the breakdown voltage. We reset the device after each sweep by applying a forward bias voltage to mitigate the effect of breakdown voltage drifts, which have been discussed in our previous work [26], though we note that the drifts occur much more slowly in our current devices. Furthermore, to ensure consistent results, the I-V measurements are repeated until the threshold voltage of consecutive sweeps are consistent within 0.1 V (usually achieved within two to three measurements); only the consistent measurements are considered in our data analysis.

Exceptions are made for input powers exceeding -20 dBm, as $I_{dev} > 200$ μA even for low V_B, far away from breakdown. Instead, we sweep V_B from 0–10 V, not increasing the bias further to avoid the risk of high I_{dev} damaging the device permanently. We also record an instance of instantaneous device failure due to high I_{dev} when input power P_{in} was increased to 7 dBm for one device. As such, all other devices were tested only up to $P_{in} = 0$ dBm.

B. RF Measurements

For RF bandwidth and eye diagram measurements, we use a single RF probe in a GS configuration (each pin contacting one of the two pads). Due to the aforementioned drift behaviour, the devices require up to a few minutes to stabilize after the bias is initally applied. Measurements are recorded only after the devices have stabilized.

The CW input laser is modulated using a 40 GHz electro-optic modulator (EOM, Eospace AZ-AV5-40-PFA-PFA-700). The EOM is operated at 65 °C to suppress the photorefractive effects. We maintain the EOM at its quadrature point, i.e. the DC bias is adjusted such that the EOM output power is at 50% of its maximum value. The RF drive is supplied by an Agilent E8363C network analyzer, which also measures the output signal from the APD, giving the RF frequency response of the devices. The measured data is corrected for the electro-optic S21 response of the EOM, and smoothed with a Savitzky–Golay filter.

For eye diagram measurements, a bit pattern generator (SHF 12104 A together with Anritsu MG3693C) is used to generate non-return-to-zero on-off keying patterns (NRZ-OOK) with pseudorandom binary sequences (PRBS) of length 2^7-1. These patterns are then amplified (Centellax OA4MVM3) and used to modulate the RF signal driving the EOM.

Conflict of Interest

The authors have no conflicts to disclose.

References

[1] A. H. Atabaki et al., "Integrating photonics with silicon nanoelectronics for the next generation of systems on a chip," *Nature*, vol. 556, no. 7701, pp. 349–354, 2018.

[2] G. Moody et al., "2022 roadmap on integrated quantum photonics," *J. Physics: Photon.*, vol. 4, no. 1, 2022, Art. no. 012501.

[3] E. Pelucchi et al., "The potential and global outlook of integrated photonics for quantum technologies," *Nature Rev. Phys.*, vol. 4, no. 3, pp. 194–208, 2022.

[4] X. Chen et al., "The emergence of silicon photonics as a flexible technology platform," *Proc. IEEE*, vol. 106, no. 12, pp. 2101–2116, Dec. 2018.

[5] V. Stojanović et al., "Monolithic silicon-photonic platforms in state-of-the-art CMOS SOI processes," *Opt. Exp.*, vol. 26, no. 10, May 2018, Art. no. 13106.

[6] S. Y. Siew et al., "Review of silicon photonics technology and platform development," *J. Lightw. Technol.*, vol. 39, no. 13, pp. 4374–4389, Jul. 2021.

[7] Y. Yuan et al., "Avalanche photodiodes on silicon photonics," *J. Semicond.*, vol. 43, no. 2, pp. 021301–021301, 2022.

[8] S. A. Srinivasan, M. Berciano, P. De Heyn, S. Lardenois, M. Pantouvaki, and J. V. Campenhout, "27 GHz silicon-contacted waveguide-coupled Ge/Si avalanche photodiode," *J. Lightw. Technol.*, vol. 38, no. 11, pp. 3044–3050, Jun. 2020.

[9] B. Wang et al., "64 Gb/s low-voltage waveguide SiGe avalanche photodiodes with distributed Bragg reflectors," *Photon. Res.*, vol. 8, no. 7, pp. 1118–1123, 2020.

[10] Y. Yuan et al., "High responsivity Si-Ge waveguide avalanche photodiodes enhanced by loop reflector," *IEEE J. Sel. Topics Quantum Electron.*, vol. 28, no. 2, pp. 1–8, Mar./Apr. 2021.

[11] D. Liu, P. Zhang, B. Tang, W. Wang, and Z. Li, "High-performance waveguide-integrated Ge/Si avalanche photodetector with lateral multiplication region," *Micromachines*, vol. 13, no. 5, 2022, Art. no. 649.

[12] T.-C. Yu, W.-T. Huang, W.-B. Lee, C.-W. Chow, S.-W. Chang, and H.-C. Kuo, "Visible light communication system technology review: Devices, architectures, and applications," *Crystals*, vol. 11, no. 9, 2021, Art. no. 1098.

[13] J. Li, P. Zou, X. Ji, X. Guo, and N. Chi, "High-speed visible light communication utilizing monolithic integrated PIN array receiver," *Opt. Commun.*, vol. 494, 2021, Art. no. 127027.

[14] R. Scott, W. Jiang, and M. J. Deen, "CMOS time-to-digital converters for biomedical imaging applications," *IEEE Rev. Biomed. Eng.*, early access, Jun. 24, 2021, doi: 10.1109/RBME.2021.3092197.

[15] H. Yang, Y. Zhang, S. Chen, and R. Hao, "Micro-optical components for bioimaging on tissues, cells and subcellular structures," *Micromachines*, vol. 10, no. 62019, Art. no. 405.

[16] C. Ciminelli, F. Dell'Olio, D. Conteduca, and M. N. Armenise, "Silicon photonic biosensors," *IET Optoelectron.*, vol. 13, no. 2, pp. 48–54, 2019.

[17] J. Haas, M. Schwartz, U. Rengstl, M. Jetter, P. Michler, and B. Mizaikoff, "Chem/bio sensing with non-classical light and integrated photonics," *Analyst*, vol. 143, no. 3, pp. 593–605, 2018.

[18] M. Kutas, B. Haase, P. Bickert, F. Riexinger, D. Molter, and G. von Freymann, "Terahertz quantum sensing," *Sci. Adv.*, vol. 6, no. 11, 2020, Art. no. eaaz8065.

[19] X. Lu et al., "Chip-integrated visible–telecom entangled photon pair source for quantum communication," *Nature Phys.*, vol. 15, no. 4, pp. 373–381, 2019.

[20] K. R. Brown, J. Chiaverini, J. M. Sage, and H. Häffner, "Materials challenges for trapped-ion quantum computers," *Nature Rev. Mater.*, vol. 6, no. 10, pp. 892–905, 2021.

[21] C. Zhang, S. Lindner, I. M. Antolović, J. Mata Pavia, M. Wolf, and E. Charbon, "A 30-frames/s, 252 SPAD flash LiDAR with 1728 dual-clock 48.8-ps TDCs, and pixel-wise integrated histogramming," *IEEE J. Solid-State Circuits*, vol. 54, no. 4, pp. 1137–1151, Apr. 2019.

[22] H. Abuella, F. Miramirkhani, S. Ekin, M. Uysal, and S. Ahmed, "ViLDAR–visible light sensing-based speed estimation using vehicle headlamps," *IEEE Trans. Veh. Technol.*, vol. 68, no. 11, pp. 10406–10417, Nov. 2019.

[23] L. You, "Superconducting nanowire single-photon detectors for quantum information," *Nanophotonics*, vol. 9, no. 9, pp. 2673–2692, 2020.

[24] I. Esmaeil Zadeh et al., "Superconducting nanowire single-photon detectors: A perspective on evolution, state-of-the-art, future developments, and applications," *Appl. Phys. Lett.*, vol. 118, no. 19, 2021, Art. no. 190502.

[25] F. Ceccarelli, G. Acconcia, A. Gulinatti, M. Ghioni, I. Rech, and R. Osellame, "Recent advances and future perspectives of single-photon avalanche diodes for quantum photonics applications," *Adv. Quantum Technol.*, vol. 4, no. 2, 2021, Art. no. 2000102.
[26] S. Yanikgonul et al., "Integrated avalanche photodetectors for visible light," *Nature Commun.*, vol. 12, 2021, Art. no. 1834.
[27] Y. Lin. et al., "Monolithically integrated, broadband, high-efficiency silicon nitride-on-silicon waveguide photodetectors in a visible-light integrated photonics platform," *Nature Commun.*, vol. 13, no. 1, pp. 1–7, 2022.
[28] S. Cuyvers et al., "Heterogeneous integration of Si photodiodes on silicon nitride for near-visible light detection," *Opt. Lett.*, vol. 47, no. 4, pp. 937–940, 2022.
[29] S. Yanikgonul, X. Luo, and G.-Q. Lo, "High-speed waveguide-integrated avalanche photodiodes for near-infrared wavelengths on SiN-on-SOI photonic platform," *J. Lightw. Technol.*, early access, Nov. 29, 2022, doi: 10.1109/JLT.2022.3225464.
[30] M. Huang et al., "56 GHz waveguide Ge/Si avalanche photodiode," in *Proc. IEEE Opt. Fiber Commun. Conf. Expo.*, 2018, pp. 1–3.
[31] J. F. Tasker et al., "Silicon photonics interfaced with integrated electronics for 9 GHz measurement of squeezed light," *Nature Photon.*, vol. 15, no. 1, pp. 11–15, 2021.
[32] X. Zeng, Z. Huang, B. Wang, D. Liang, M. Fiorentino, and R. G. Beausoleil, "Silicon–germanium avalanche photodiodes with direct control of electric field in charge multiplication region," *Optica*, vol. 6, no. 6, pp. 772–777, 2019.
[33] S. Yanikgonul, V. Leong, J. R. Ong, C. E. Png, and L. Krivitsky, "Simulation of silicon waveguide single-photon avalanche detectors for integrated quantum photonics," *IEEE J. Sel. Topics Quantum Electron.*, vol. 26, no. 2, pp. 1–8, Mar./Apr. 2020.
[34] S. Yanikgonul, V. Leong, J. R. Ong, C. E. Png, and L. Krivitsky, "2D monte carlo simulation of a silicon waveguide-based single-photon avalanche diode for visible wavelengths," *Opt. Exp.*, vol. 26, no. 12, pp. 15232–15246, 2018.
[35] A. R. Schaefer, E. F. Zalewski, and J. Geist, "Silicon detector nonlinearity and related effects," *Appl. Opt.*, vol. 22, no. 8, pp. 1232–1236, 1983.
[36] K. Stock, S. Morozova, L. Liedquist, and H. Hofer, "Nonlinearity of the quantum efficiency of Si reflection trap detectors at 633 nm," *Metrologia*, vol. 35, no. 4, 1998, Art. no. 451.
[37] M. Tanabe, K. Amemiya, T. Numata, and D. Fukuda, "Spectral supralinearity of silicon photodiodes in visible light due to surface recombination," *Appl. Opt.*, vol. 55, no. 11, pp. 3084–3089, 2016.
[38] M. Tanabe and K. Kinoshita, "Supralinear behavior and its wavelength dependence of silicon photodiodes with over-filled illumination in visible range," *Appl. Opt.*, vol. 57, no. 13, pp. 3575–3580, 2018.
[39] H. Zhu, L. Zhou, X. Sun, Y. Zhou, X. Li, and J. Chen, "On-chip optical power monitor using periodically interleaved PN junctions integrated on a silicon waveguide," *IEEE J. Sel. Topics Quantum Electron.*, vol. 20, no. 4, pp. 56–63, Jul./Aug. 2014.
[40] H. Zhu, K. Goi, and K. Ogawa, "All-silicon waveguide photodetection for low-bias power monitoring and 20-km 28-Gb/s NRZ-OOK signal transmission," *IEEE J. Sel. Topics Quantum Electron.*, vol. 24, no. 2, pp. 1–7, Mar./Apr. 2018.
[41] L. Virot et al., "High-performance waveguide-integrated germanium PIN photodiodes for optical communication applications," *Photon. Res.*, vol. 1, no. 3, pp. 140–147, 2013.
[42] W. S. Zaoui et al., "Frequency response and bandwidth enhancement in Ge/Si avalanche photodiodes with over 840 GHz gain-bandwidth-product," *Opt. Exp.*, vol. 17, no. 15, pp. 12641–12649, 2009.
[43] A. Chatterjee et al., "High-speed waveguide integrated silicon photodetector on a SiN-SOI platform for short reach datacom," *Opt. Lett.*, vol. 44, no. 7, pp. 1682–1685, 2019.
[44] M. M. P. Fard, C. Williams, G. Cowan, and O. Liboiron-Ladouceur, "High-speed grating-assisted all-silicon photodetectors for 850 nm applications," *Opt. Exp.*, vol. 25, no. 5, pp. 5107–5118, 2017.
[45] B. Tossoun, G. Kurczveil, S. Srinivasan, A. Descos, D. Liang, and R. G. Beausoleil, "32 Gbps heterogeneously integrated quantum dot waveguide avalanche photodiodes on silicon," *Opt. Lett.*, vol. 46, no. 16, pp. 3821–3824, 2021.
[46] Y. Xiang, H. Cao, C. Liu, J. Guo, and D. Dai, "High-speed waveguide Ge/Si avalanche photodiode with a gain-bandwidth product of 615 GHz," *Optica*, vol. 9, no. 7, pp. 762–769, 2022.
[47] J. Zhang et al., "First Si-waveguide-integrated InGaAs/InAlAs avalanche photodiodes on SOI platform," in *Proc. IEEE Symp. VLSI Technol. Circuits*, 2022, pp. 409–410.